Simultaneous Two-Colour Two-Dye Thermometry PLIF and PIV to Determine the Nusselt Number in Steady and Oscillatory Poiseuille-Rayleigh-Bénard Convection

Sina Kashanj and David S. Nobes*
Dept. of Mechanical Engineering, University of Alberta, Canada
* Correspondent author: dnobes@ualberta.ca

Keywords: PLIF, PIV, Poiseuille-Rayleigh-Bénard convection

ABSTRACT

In a flow field driven by natural or mixed convection, the measurement of heat transfer and hence the Nusselt number, requires simultaneous measurement of the vertical component of velocity and the vertical temperature gradient. The spatiotemporal nature of the formation of large-scale circulating structures, their interaction with the cross flow and its impact on heat transport, temperature distribution and wall shear stress also can be identified by simultaneous velocimetry and thermometry. An optical measurement system has been developed to apply a high sensetive (~7 %/°C) two-colour two-dye planar laser-induced fluorescence (PLIF) and particle image velocimetry (PIV) to identify the flow and temperature organization and measure the heat transfer and wall shear stress. The system is to be used to investigate a Poiseuille-Rayleigh-Bénard convection system designed and fabricated to operate in both continuous and oscillatory conditions. The aim is to allow investigation of the influence and effect of large-scale flow structures and thermal plumes on heat and flow transport properties.

1. Introduction

Large-scale circulating structures (LSC) have a significant role in heat and momentum transfer in wall-bounded turbulent buoyancy-driven flows (Zwirner et al., 2020). For natural convection in an enclosure heated from below and cooled from above, known as Rayleigh-Bénard convection (RBC), the formation of LSC leads to an enhancement in heat and momentum transport properties (Zwirner et al., 2020). Turbulent RBC is significantly unsteady and the number and scale of the circulating structures varies temporally affecting the state of the flow (Zwirner et al., 2020). Mixed convection in a wall-bounded flow heated from below is known as Poiseuille-Rayleigh-Benard convection (PRBC) (Maughan & Incropera, 1987). In PRBC, it is shown that the formation of LSC is a spatiotemporal phenomenon which is a function of the length of the heated channel as well as the development time (Maughan & Incropera, 1987). Although the formation of LSC in PRBC can enhance heat transfer, in real applications it is suppressed due to the short length of the heated channel and temporal unsteadiness (Maughan & Incropera, 1987). An important case with temporal unsteadiness is a reciprocating flow in which the formation of the LSC could be suppressed due to the acceleration and deceleration of the flow (Maughan & Incropera, 1987).

The Nusselt number can be defined as:

$$Nu(t) = \frac{[\langle u_z T \rangle - \alpha \langle \partial_z T \rangle]}{(\alpha \Delta T / h)} \tag{1}$$

where $\langle \cdot \rangle$ denotes the spatial average, α is thermal diffusivity, T is the temperature and h is the height of the convection cell. In this equation, z is also the direction normal to the hot boundary and u_z is the vertical velocity component. As can be seen in this equation, to calculate the heat transfer coefficient, Nusselt number measurement of both the temperature of the whole flow field and velocity field is required. The role of LSC in RBC flow has been a focus of interest in the last decade, yet there is not a coherent understanding of the effect of LSC in mixed convection.

This work is an experimental investigation on the flow of Poiseuille-Rayleigh-Bénard flow in mixed convection regime. This experimental study is undertaken for both continuous and reciprocating flows. In this abstract, the integration of a relatively high sensitive two-colour PLIF for thermometry and PIV for velocimetry is briefly discussed. Sample results visualizing and measuring the temperature and velocity of the designed and fabricated PRBC system is also represented. At the end, an outline of the final version of the paper and presentation is introduced.

2. Methodology

Experimental Setup

Based on the properties of the PRBC flow a fluid test rig has been designed and fabricated. A rendering of the fluid test rig is depicted in Figure 1(a). This fluid test rig is designed to provide the test condition for both continuous and oscillatory flow. As can be seen in Figure 1(a), an actuator which is a cylindrical piston drives the flow inside the flow test rig. The actuator is controlled by a traverse which has been driven by a high precision low noise motor (ClearPath-SD, Teknik, Inc.) to provide different types of motion including the oscillatory and continuous flow which are the purpose of this work.

The test section shown in Figure 1(b) is a rectangular channel with a cross-section with the height of $h = 10$ mm and width of $w = 55$ mm. The test section is made from an acrylic sheet with a thickness of 6.35 mm that has a low thermal conduction coefficient of 0.2 W/mK. This test section has been designed to have maximum possible optical access, hence both side walls and the top wall of the test section is made from acrylic sheet. The bottom of the test section is featured by a heat exchanger with a relatively thin copper sheet transferring the heat from a channel underneath to the test section containing the working fluid, which is water in this case. This heat exchanger is connected to a water bath to control the temperature and provide the temperature constant boundary condition at the bottom wall of the test section. The heat exchanger and the support bases of the test section are made using an SLA 3D printer (Form3, Formlabs Inc.) and printing material, a liquid photopolymer, with a low thermal conduction coefficient of 0.15 W/mK.

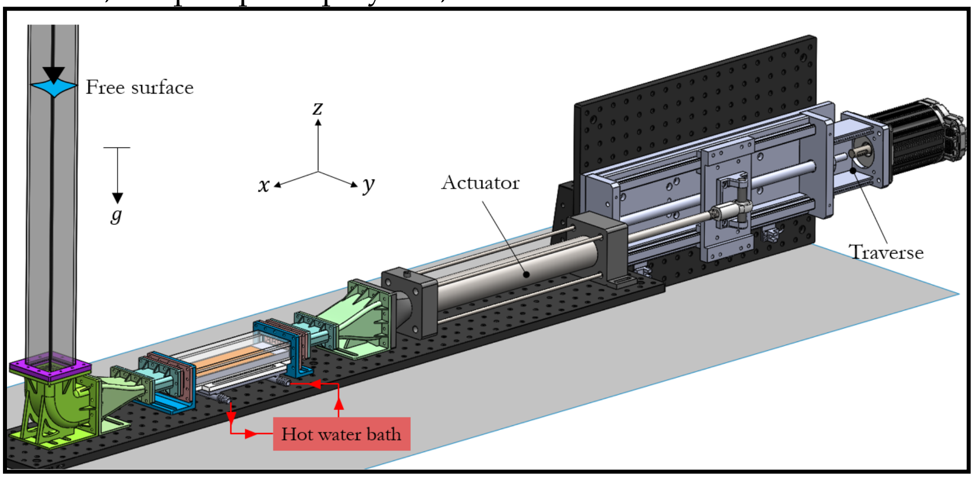

(a)

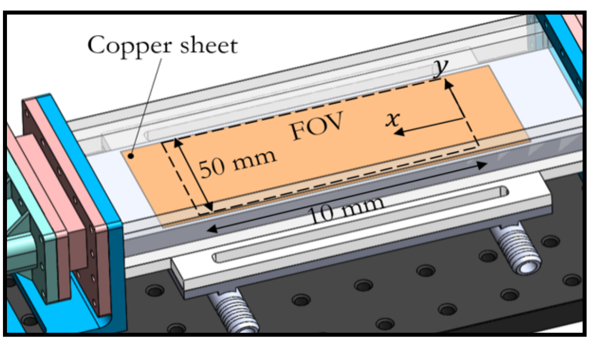

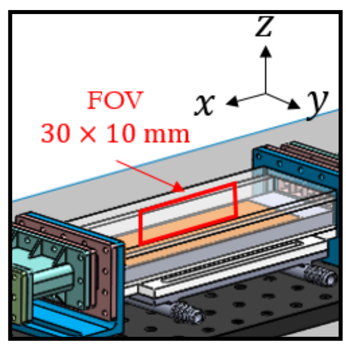

(b) (c)

Figure 1. (a) Rendering of the solid model of the fluid test rig designed and fabricated to generate continuse and oscillatory flows. (b) Depicts the test section properties and the field of view, FOV in $x - y$ plane; FOV1. (c) FOV properties in $x - z$ plane; FOV2.

The field of view for measuring the velocity and temperature are depicted in Figure 1(b) and (c). The first field of view, FOV1 is located in $x - y$ plane as is shown in Figure 1(b). The height of the field of view varies from the bottom wall at $z/h = 0$, to the top wall at $z/h = 1$. The second field of view, FOV2 is in the $x - z$ plane as is shown in Figure 1(cPIV

A schematic of the optical measurement system integrated to capture the velocity field at FOV2 is shown in Figure 2. As can be seen in this figure, fluorescent particles with a diameter of 3.2 μm and maximum absorption and emission spectrum of 546 and 576 nm are used as seeding particles. A raw image of the fluid domain with seeding particles being illuminated by a 532 nm laser and captured by a long pass filter, $\lambda > 600$ nm is shown in Figure 2. The laser sheet is generated using Scanning mirror 1. Scanning mirror 2 is used to set the location of the laser sheet in the y-direction. The laser sheet is collimated using a double-convex lens and reflected to the $x - z$ plane by a mirror. The sample result using this system is the velocity vectors of the Poiseuille flow shown earlier in Figure 5. To apply PIV a commercial Software (DaVis 10.0.5, LaVision GmbH) is used. The velocity vectors are calculated by a multi-pass iteration with the minimum interrogation size of 32 pixel × 32 pixel with 75% overlap.

(a)

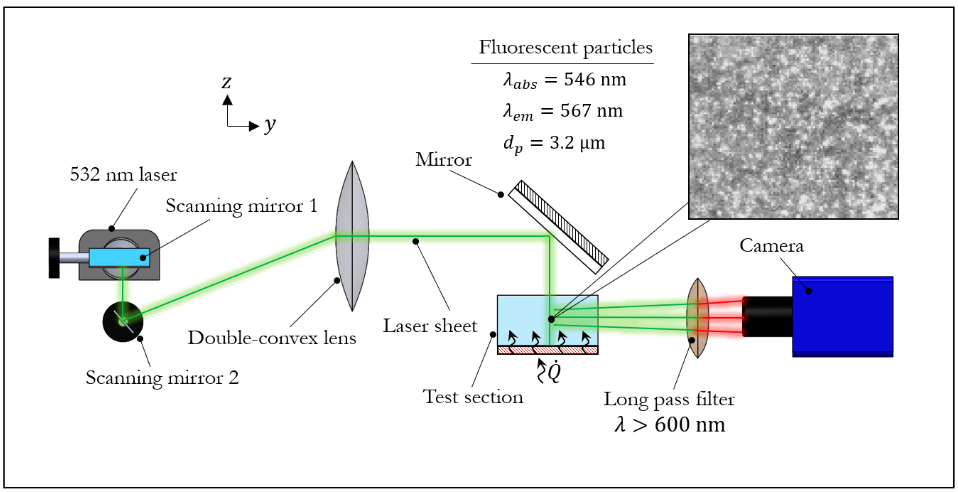

(b)

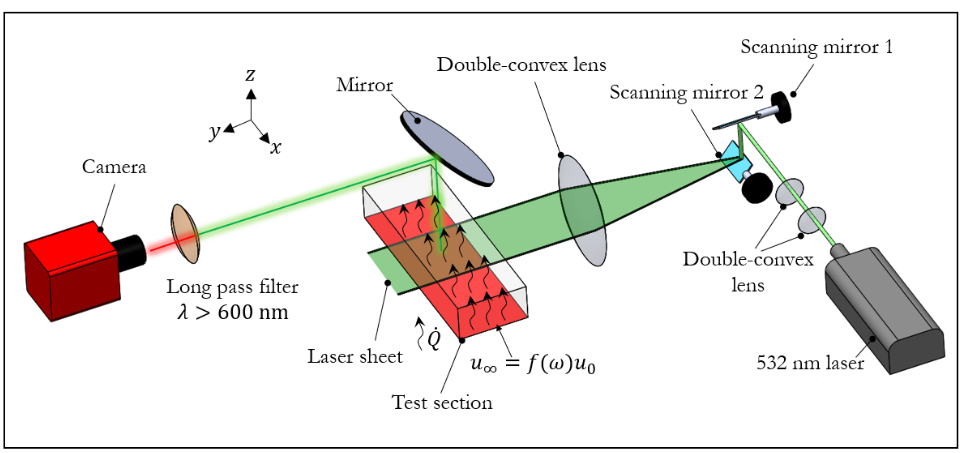

Figure 2. Schematic of the optical measuement system used to apply PIV for (a) FOV2 and (b) FOV1.

PLIF

A schematic of the optical measurement system used to apply two-colour PLIF and capture the temperature field of FOV1 is illustrated in Figure 1(a). To apply two-colour PLIF a 532 nm laser was used. Two scanning mirrors were also used to generate the laser sheet and to scan the volume of the test section in the z-direction. Two fluorescent dyes of Fluorescein (Fl) and Kiton red (Kr) were used to apply two-colour PLIF. For each fluorescent dye a camera with a set of optical filters were used to collect the temperature sensitive signal of each dye. More details of the applied technique for the thermometry can be found in (Kashanj & Nobes, 2023, 2024) in which development and enhancing the temperature sensetivity, ~7%/℃ of a PLIF for thermometry purposes is discussed.

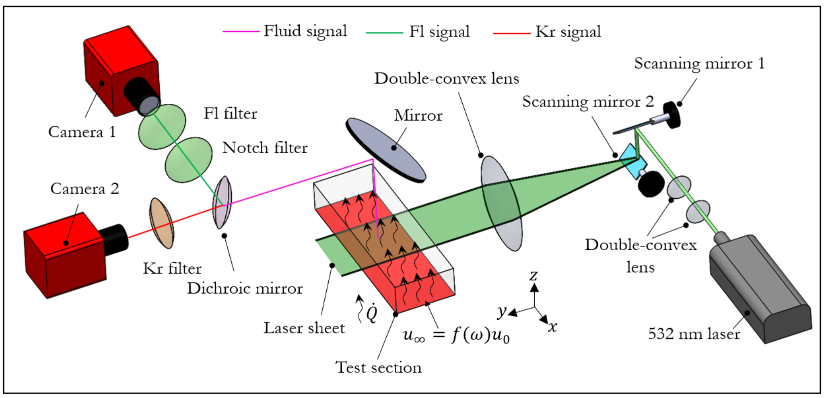

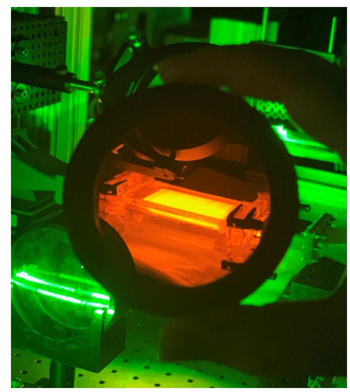

(a) (b)

Figure 3. (a) Schematic of the optical measuement system used to apply two-colour two-dye PLIF in FOV1. (b) Shows the test section and emmitted light from the two-dye while it is illuminated by the 532 nm laser sheet.

3. Results

Temperature field

For FOV1, a sample result of the temperature field captured by applying the two-colour PLIF at z = 9 mm is shown in Figure 4(a). This temperature map shows the temperature field at the start of convection at $Ra = 2 \times 10^7$ while $Re = 0$ highlighting the zero cross-flow in this case. The temperature map indicates the rise of the thermal plumes and their development in the $x - y$ direction which leads to an increase in the temperature of the flow field. On the right-hand side of the temperature map the thermal plumes can be seen while on the left-hand side the uniform temperature shows the ambient temperature. The start of the convection from the right-hand side and its spatial development to the left is due to the configuration of the heat exchanger in which the inlet of the water bath is at the right and the outlet is at the left. The temporal evolution of the temperature field which is along with the increase in the temperature can be seen in Figure 4(b) which is at $t = 23$ s. This visualization and capturing the thermal plumes spatial and temporal development highlights both high sensitivity and short response time of the used PLIF.

Velocity field

For FOV2, the vorticity field along to the calculated velocity vectors is shown in Figure 5(a) at the continuous flow condition and Reynolds number of $Re = 25$; where $Re \equiv \bar{u}\, h/\nu$, $\bar{u}$ is the axial mean velocity and ν is the kinematic viscosity. The velocity profile of the dimensionless axial velocity u_x^* along the center of the channel i.e. $x/h = 0$ line is depicted in Figure 5(b) highlighting the laminar Poiseuille flow.

(a)

(b)

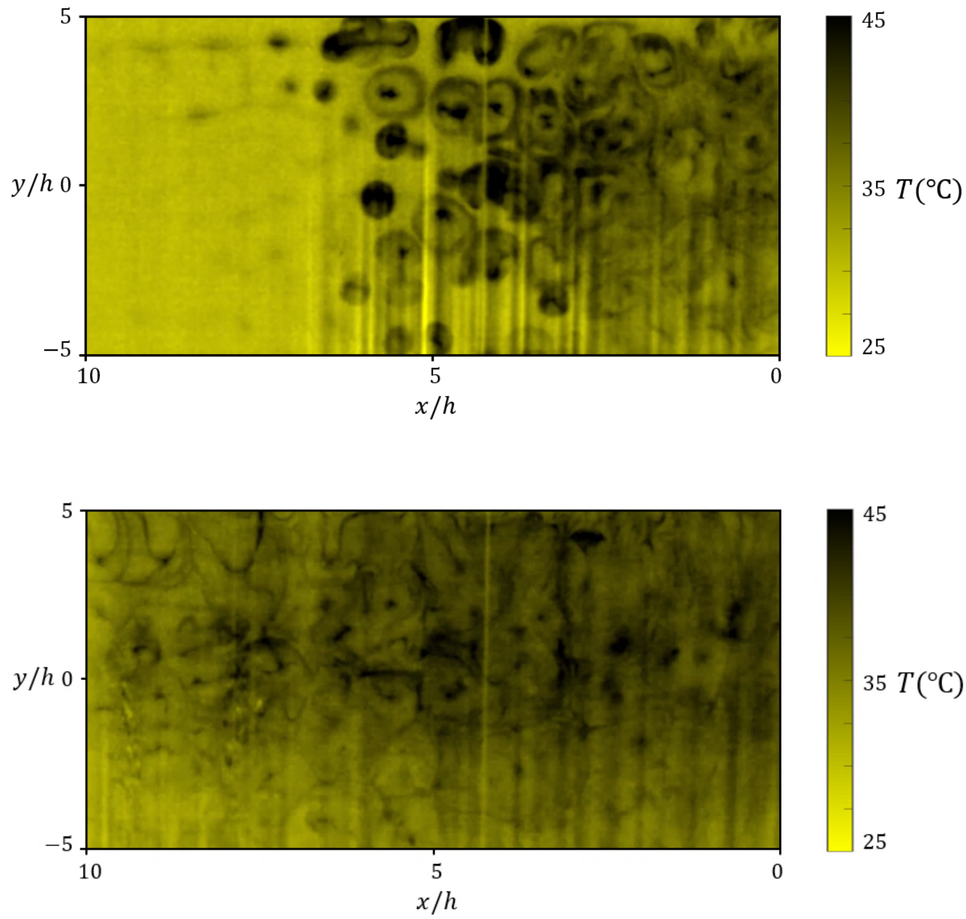

Figure 4. Temperature map of the PRBC flow from FOV1 at the test section height of $z = 9$ mm. $Ra = 2 \times 10^7$ and $Re = 0$. (a) $t \approx 5$ s (b) $t \approx 23$ s.

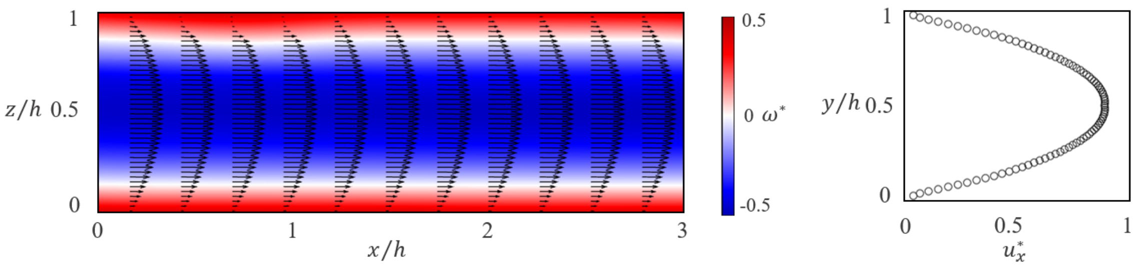

(a) (b)

Figure 5. (a) velocity field of the axial flow, u_x^* corresponding to FOV2 for the Poiseuille flow while $Re = 25$, and $Ra = 0$. (b) Velocity profile, u_x^* along the $x/h = 0$ line.

The experiment for the continuous flow includes three conditions. The first condition is at $Re = 0$ i.e. zero cross-flow. In this condition which is resembling the Rayleigh-Bénard flow, the convection starts with the rise of thermal plumes from the bottom boundary with the constant temperature. The boundary condition is illustrated in Figure 6(a) in which the red and blue arrows represent the flow passing in the vicinity of the bottom (hot) and top (adiabatic) boundaries, respectively. This flow is generated due to the formation of LSCs in the system.

(a)

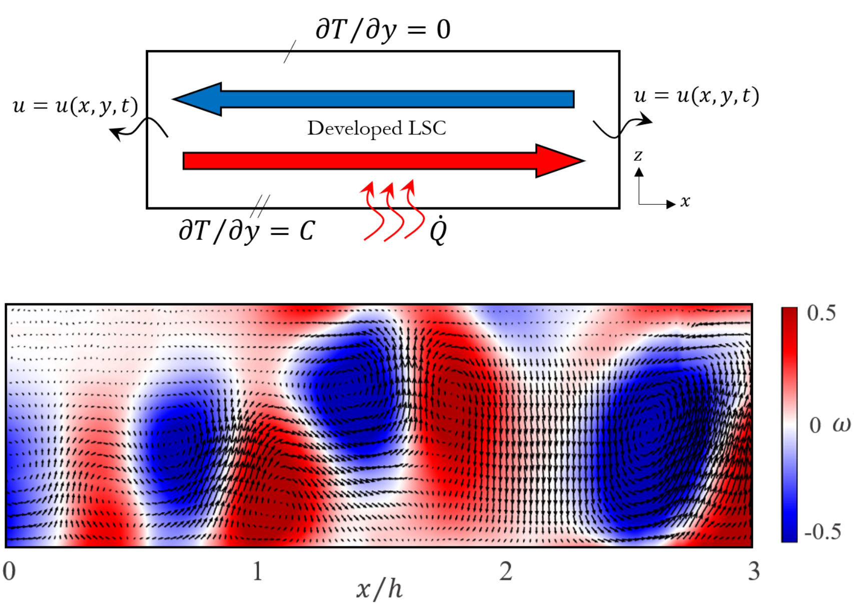

(b)

(c)

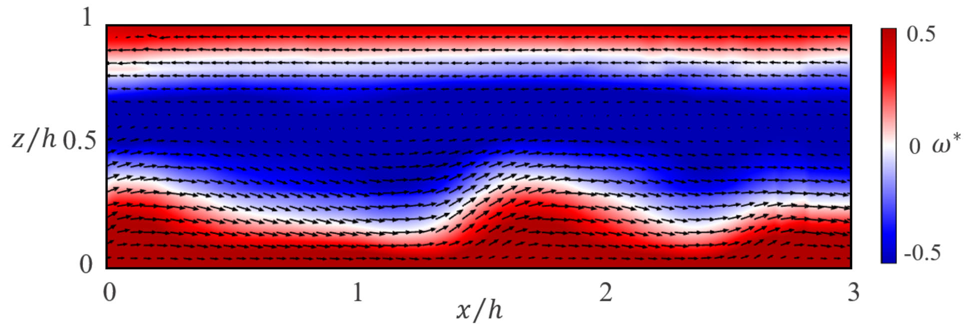

Figure 6. (a) Schematic of the boundary condition while flow is captured in FOV2 (b) Instantaneous vorticity field and velocity vectors at the start of the convection (c) Instantaneous vorticity field and velocity vectors of the developed flow. $Re = 0$ and $Ra = 2 \times 10^7$.

(a)

(b)

(c)

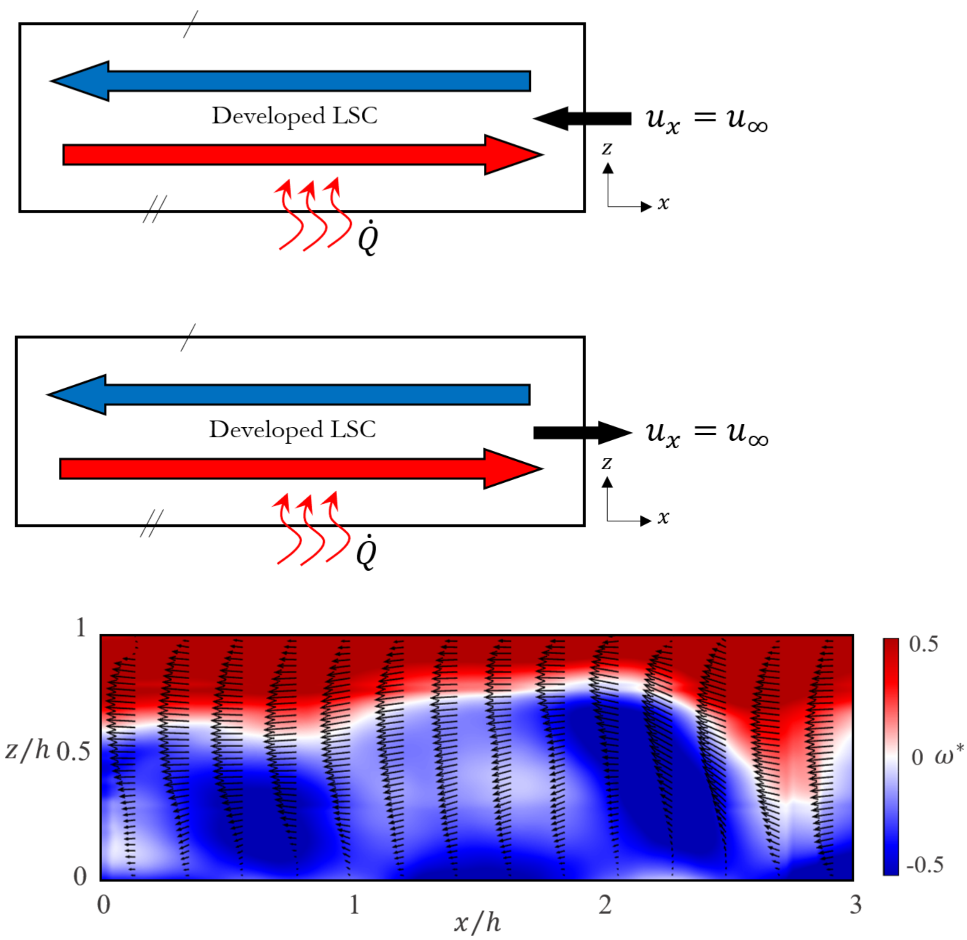

(d)

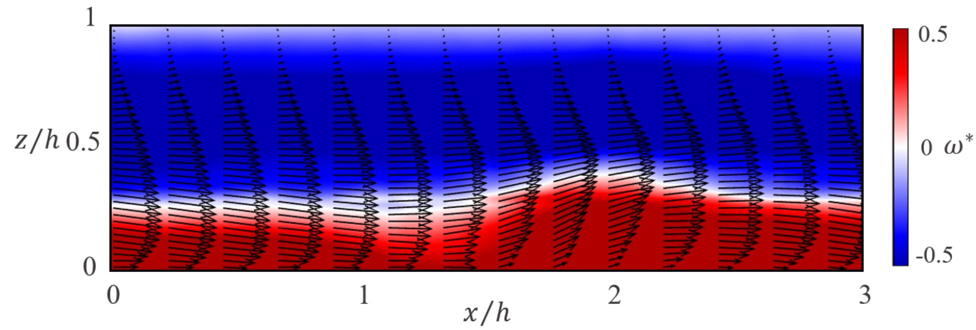

Figure 7. (a), (b) Schematic of the boundary condition for two different direction of the cross-flow while flow is captured in FOV2. (c) Instantaneous vorticity field and velocity vectors corresponding to boundary condition in (a). (d) Instantaneous vorticity field and velocity vectors corresponding to boundary condition in (b). For both cases $Re = 75$ and $Ra = 2 \times 10^7$.

The start of the convection and formation of the preliminary thermal plumes can be seen in Figure 6(b) representing the instantaneous vorticity map and the velocity vectors at $t = 12.3$ s. The developed flow for this case at $t = 210.6$ s is shown in Figure 6(c). The instantaneous vorticity map and the velocity vectors of the developed flow highlight the formation of the LSC. While the flow in the vicinity of the top wall is resembling the Poiseuille flow shown in Figure 5(a), it can be seen that the flow in the vicinity of the bottom wall is disrupted by the vertical component of the velocity induced due to the formation of thermal plumes. This existence of the vertical component of the velocity near the wall with heat transfer highlights the importance of the measurement of the velocity along with the temperature gradient for calculating the true heat transfer coefficient of the system.

The second and third condition of the experiment is considered by introducing the cross-flow to the system discussed above for Figure 6. As is illustrated in Figure 7(a) and (b), introducing the cross-flow could be either along or opposite to the direction of the flow above the bottom boundary. This is important as LSC is generated and maintained by the formation of hot thermal plumes from the bottom boundary. A sample result of the flow field shown by the instantaneous vorticity field and velocity vectors is shown in Figure 7(c) and (d). For both cases, the Reynolds number is equal to $Re = 75$ and Rayleigh number equal to $Ra = 2 \times 10^7$ while the direction of the cross-flow is opposite to the direction of the flow in the vicinity of the bottom boundary in Figure 7(c) and it is in the same direction the flow in the vicinity of the bottom boundary at Figure 7(d). As can be seen, besides the overall direction of the flow, the instantaneous vorticity field and velocity vectors are representing quite different physics from the typical Poiseuille flow and the flow resembling the Rayleigh-Bénard flow shown in Figure 6(c). For Figure 7(c), formation of regions with high negative vorticity which are formed due to the impinging of the thermal plumes with the cross-flow is noticeable. For Figure 7(d), while the maximum velocity is moved down to $z/h < 0.5$, a relatively thick stagnation region is formed near the top wall (adiabatic boundary). The cycle dependent velocity map of the flow at the mid-height of the test section, $z = 5$ mm can be seen in Figure 8(a) for four different phases of $\omega = \pi/2\,, \pi, 3\pi/2,$ and 2π where $\omega = 2\pi/T$ and T is the period of oscillation. Results shown in Figure 8 are also at the peak Reynolds number of $Re_p = 80$, and Womersly number of $\alpha = 8.4$, where $\alpha \equiv h\sqrt{\omega/4\nu}$ and $Re_p \equiv u_m h/\nu$. In these two definitions, u_m is the maximum velocity, and ν is the kinematic viscosity of the working fluid. As can be observed in $\omega = \pi/2$ and $\omega = 3\pi/2$, flow is at the peak of the acceleration phase at two different directions which occurs before the start of the deceleration. Two other phases of $\omega = 0$ and $\omega = \pi$ in Figure 2(a) show the start of the acceleration in two different directions. The stagnation line at $y^* = y/h = 0.35$ can be observed for both phases, $\omega = \pi$ and $\omega = 2\pi$. The velocity profile of u_x along the width of the channel, y-direction is shown in Figure 2(b) for a single cycle of reciprocation, $0 \leq \omega < 2\pi$. The red colour plots depict the velocity profile of the four velocity contours shown in Figure 2(a). The stagnation line also can be seen in this figure for $\omega = 0$ and $\omega = \pi$ showing the start of the reverse flow direction.

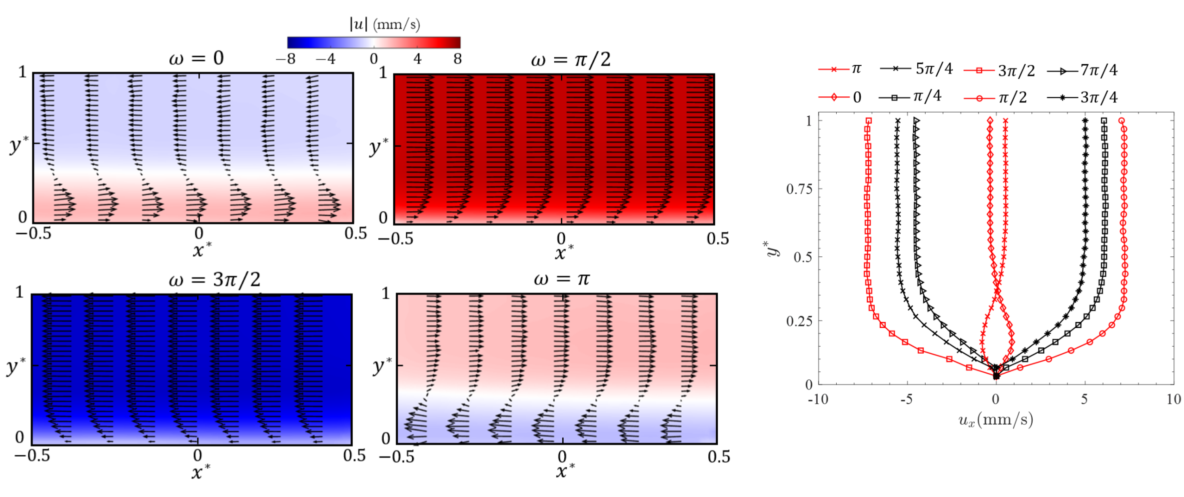

(a) (b)

Figure 8. (a) Contour of the velocity magnitude in $x - y$ plane at the midheight of the test section, z=5 mm at the four different phases of $\omega = \pi/2$, $\omega = \pi$, $\omega = 3\pi/2$, and $\omega = 2\pi$. (b) Velocity profile, u_x along the width of the channle, y for different phases of reciprocating flow; red colour denotes the phases that are shown as velcoity contours in (a).

Conclusion

The development and application of planar laser-induced fluorescence (PLIF) thermometry combined with particle image velocimetry (PIV) was demonstrated in this paper. This system was developed to understand the heat transfer mechanism in convection-driven flow fields such as Poiseuille-Rayleigh-Bénard convection (PRBC). This optical measurement system allows for the simultaneous measurement of the vertical velocity component and the vertical temperature gradient, essential for determining the Nusselt number and analysing the spatial and temporal formation of flow vortical structures. The design and fabrication of the PRBC flow test rig for running both steady and oscillatory flow was discussed as well.

References

Adrian, B. (2013). *CONVECTION HEAT TRANSFER*. John Wiley and Sons, Inc.

Bown, M. R., MacInnes, J. M., & Allen, R. W. K. (2007). Three-component micro-PIV using the continuity equation and a comparison of the performance with that of stereoscopic measurements. *Experiments in Fluids*, *42*(2), 197–205. https://doi.org/10.1007/s00348-006-0229-3

Coppeta, J., & Rogers, C. (1998). Dual emission laser induced fluorescence for direct planar scalar behavior measurements. *Experiments in Fluids*, *25*(1), 1–15. https://doi.org/10.1007/s003480050202

Doering, C. R. (2019). Thermal forcing and 'classical' and 'ultimate' regimes of Rayleigh–Bénard convection. *Journal of Fluid Mechanics*, *868*, 1–4. https://doi.org/10.1017/JFM.2019.118

Estrada-Pérez, C. E., Hassan, Y. A., & Tan, S. (2011). Experimental characterization of temperature sensitive dyes for laser induced fluorescence thermometry. *Review of Scientific Instruments*, *82*(7), 74901. https://doi.org/10.1063/1.3590929

Hishida, K., & Sakakibara, J. (2000). Combined planar laser-induced fluorescence-particle image velocimetry technique for velocity and temperature fields. *Experiments in Fluids*, *29*(SUPPL. 1). https://doi.org/10.1007/s003480070015

Horstmann, G. M., Schiepel, D., & Wagner, C. (2018). Experimental study of the global flow-state transformation in a rectangular Rayleigh-Bénard sample. *International Journal of Heat and Mass Transfer*, *126*, 1333–1346. https://doi.org/10.1016/j.ijheatmasstransfer.2018.05.097

Kashanj, S., & Nobes, D. S. (2021a). Application of simultaneous time-resolved 3-D PTV and Two Colour LIF in Studying Rayleigh-Benard Convection. *14th International Symposium on Particle Image Velocimetry*, *1*(1). https://doi.org/10.18409/ISPIV.V1I1.164

Kashanj, S., & Nobes, D. S. (2021b). Investigation Into The Onset Of Turbulent Rayleigh-Benard Convection Using Time-Resolved 2-D Particle Image Velocimetry. *Progress in Canadian Mechanical Engineering*. https://doi.org/10.32393/CSME.2021.91

Kazemi, M. A., Nobes, D. S., & Elliott, J. A. W. (2018). Investigation of the phenomena occurring near the liquid-vapor interface during evaporation of water at low pressures. *Physical Review Fluids*, *3*(12), 1–27. https://doi.org/10.1103/PhysRevFluids.3.124001

Khodakov, D., Li, J., Zhang, J. X., & Zhang, D. Y. (2021). Highly multiplexed rapid DNA detection with single-nucleotide specificity via convective PCR in a portable device. *Nature Biomedical Engineering 2021 5:7*, *5*(7), 702–712. https://doi.org/10.1038/s41551-021-00755-4

Kim, H. J., & Kihm, K. D. (2001). Application of a two-color laser induced fluorescence (LIF) technique for temperature mapping. *American Society of Mechanical Engineers, Heat Transfer Division, (Publication) HTD*, *369*(7), 335–341.

Lohse, D., & Xia, K. Q. (2010). Small-scale properties of turbulent rayleigh-benard convection. *Annual Review of Fluid Mechanics*, *42*, 335–364. https://doi.org/10.1146/annurev.fluid.010908.165152

Martin, J. E., & García, M. H. (2009). Combined PIV/PLIF measurements of a steady density current front. *Experiments in Fluids*, *46*(2), 265–276. https://doi.org/10.1007/s00348-008-0556-7

Sakakibara, J., & Adrian, R. J. (1999). Whole field measurement of temperature in water using two-color laser induced fluorescence. *Experiments in Fluids*, *26*(1–2), 7–15. https://doi.org/10.1007/s003480050260

Shafii, M. B., Lum, C. L., & Koochesfahani, M. M. (2010). In situ LIF temperature measurements in aqueous ammonium chloride solution during uni-directional solidification. *Experiments in Fluids*, *48*(4), 651–662. https://doi.org/10.1007/s00348-009-0758-7

Song, X., & Nobes, D. S. (2011). Experimental investigation of evaporation-induced convection in water using laser based measurement techniques. *Experimental Thermal and Fluid Science*, *35*(6), 910–919. https://doi.org/10.1016/j.expthermflusci.2011.01.010

Sutton, J. A., Fisher, B. T., & Fleming, J. W. (2008). A laser-induced fluorescence measurement for aqueous fluid flows with improved temperature sensitivity. *Experiments in Fluids*, *45*(5), 869–881. https://doi.org/10.1007/s00348-008-0506-4

Zwirner, L., Tilgner, A., & Shishkina, O. (2020). Elliptical Instability and Multiple-Roll Flow Modes of the Large-Scale Circulation in Confined Turbulent Rayleigh-Bénard Convection. *Physical Review Letters*, *125*(5), 54502. https://doi.org/10.1103/PhysRevLett.125.054502.

Kashanj, S., & Nobes, D. S. (2023). Application of 4D two-colour LIF to explore the temperature field of laterally confined turbulent Rayleigh–Bénard convection. *Experiments in Fluids*, *64*(3). https://doi.org/10.1007/s00348-023-03589-9

Kashanj, S., & Nobes, D. S. (2024). Temperature field of non-Oberbeck-Boussinesq Rayleigh-Bénard convection in a low aspect ratio cell. *Physics of Fluids*, *36*(4). https://doi.org/10.1063/5.0197275